RESEARCH ARTICLE

ADVANCED ELECTRONIC MATERIALS
www.advelectronicmat.de

Check for updates

A Self-Powered CNT–Si Photodetector with Tuneable Photocurrent

Aniello Pelella, Daniele Capista, Maurizio Passacantando, Enver Faella, Alessandro Grillo, Filippo Giubileo, Nadia Martucciello, and Antonio Di Bartolomeo**

A photodetector with bias-tuneable current is realized by adding a film of single-walled carbon nanotubes (CNT), forming a CNT/Si_3N_4/Si capacitor, to a prefabricated Pt–Ti/Si_3N_4/Si metal–insulator–semiconductor (MIS) diode. Electrical characterization of the entire device is performed to extract the temperature-dependent ideality factor and Schottky barrier height in the framework of the thermionic emission theory. The CNT/Si_3N_4/Si capacitor increases the reverse current of the parallel Pt–Ti/Si_3N_4/Si MIS diode by adding a Fowler–Nordheim tunneling current at high reverse voltage bias. This feature endows the photodetector with two different photocurrent levels, photoresponsivity up to 370 mA W^{-1} and external quantum efficiency up to 50% at 950 nm wavelength. The device also shows a different photoresponse when light is focused on the CNT/Si_3N_4/Si region or around the Pt–Ti/Si_3N_4/Si structure. The photodetector can also be used as an optoelectronic Boolean logic device, in which the applied voltage bias and the incident light are the two input signals, and the photocurrent is the output. Furthermore, light generates a photocurrent at zero voltage and a photovoltage at zero current, making the device a self-powered photodetector.

1. Introduction

Due to their excellent properties,[1–3] CNTs are suitable for several applications, from fillers of composite materials[4–6] to chemical and biomedical sensors,[7–9] or to improve the electronic and optical properties of devices.[10–15] As other nano-structured materials,[16–19] CNTs have been widely used for photodetection.[20,21]

CNT photodetectors have a high dark current due to the high electrical conductivity of the nanotubes. However, this issue can be overcome by combining the CNTs with semiconductors like silicon to form heterostructures that suppress the dark current and lead to highly sensitive hybrid photodetectors.[21–26] Moreover, the atomic-level interface between CNT and silicon facilitates charge separation and transfer due to few disordered states at the interface. Therefore, these heterostructures have received much attention in the last several years.[27–31]

The CNT/Si heterostructures often include an insulating inter-layer that plays an important role in the optoelectronic properties of the device by eliminating the pinning of the Fermi level.[32–34] Indeed, it has been shown that the presence of an insulating interlayer affects the current–voltage (I–V) and capacitance–voltage characteristics of any metal–semiconductor structure[15] and enhances its photodetection capability.[35–40] For instance, Jia et al. showed that the formation of an oxide layer at the interface of a CNT/Si heterostructure switches charge transport from thermionic emission to a mixture of thermionic emission and tunneling and improves the overall diode properties.[41] Filatzikioti et al. fabricated a hybrid multiwalled CNT/Si_3N_4/n-Si photodetector with adequate responsivity in the UV and visible part of the spectrum and promising for the IR region due to the CNT bandgap.[42]

Besides photodetection, a CNT/Si device can be used also in heterogeneous logic circuits,[43] such as Boolean optoelectronic circuits. Y.L. Kim et al. proposed a logic device based on a single-walled CNT/Si heterojunction photodiode, in which the optical and electrical inputs can control the output current.[44]

In this work, we use single-walled CNTs to realize a CNT/Si_3N_4/Si capacitor with enhanced capacitance due to the high dielectric constant of Si_3N_4 (≈7.5). The CNT/Si_3N_4/Si capacitor is in parallel to a pre-existing Pt–Ti/Si_3N_4/Si structure, that becomes a MIS diode after electrical stress. The electric transport

A. Pelella, E. Faella, A. Di Bartolomeo
Department of Physics and Interdepartmental Centre NanoMates
University of Salerno
via Giovanni Paolo II, Fisciano, Salerno 84084, Italy
E-mail: apelella@unisa.it; adibartolomeo@unisa.it

A. Pelella, E. Faella, F. Giubileo, N. Martucciello, A. Di Bartolomeo
CNR-SPIN
via Giovanni Paolo II, Fisciano, Salerno 84084, Italy

D. Capista, M. Passacantando
Department of Physical and Chemical Science
University of L'Aquila
Via Vetoio, Coppito 67100, L'Aquila, Italy

M. Passacantando
CNR-SPIN L'Aquila
Via Vetoio, Coppito 67100, L'Aquila, Italy

A. Grillo
Department of Chemistry
University of Manchester
Manchester M13 9PL, UK

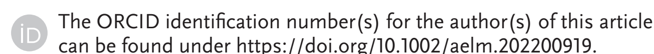
The ORCID identification number(s) for the author(s) of this article can be found under https://doi.org/10.1002/aelm.202200919.

© 2022 The Authors. Advanced Electronic Materials published by Wiley-VCH GmbH. This is an open access article under the terms of the Creative Commons Attribution License, which permits use, distribution and reproduction in any medium, provided the original work is properly cited.

DOI: 10.1002/aelm.202200919

2199160x, 2023, 1, Downloaded from https://onlinelibrary.wiley.com/doi/10.1002/aelm.202200919 by Cochraneltalia, Wiley Online Library on [28/02/2023]. See the Terms and Conditions (https://onlinelibrary.wiley.com/terms-and-conditions) on Wiley Online Library for rules of use; OA articles are governed by the applicable Creative Commons License

2199160x, 2023, 1, Downloaded from https://onlinelibrary.wiley.com/doi/10.1002/aelm.202200919 by CochraneItalia, Wiley Online Library on [28/02/2023]. See the Terms and Conditions (https://onlinelibrary.wiley.com/terms-and-conditions) on Wiley Online Library for rules of use; OA articles are governed by the applicable Creative Commons License

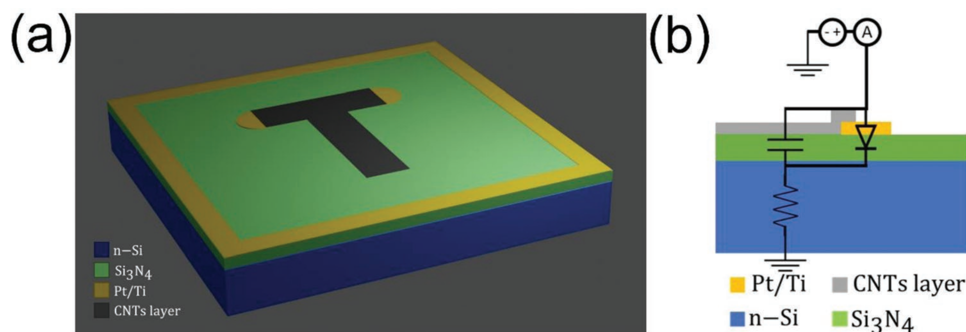

Figure 1. a) 3D schematic view and b) cross-section of the device under study.

through the entire device is investigated as a function of the temperature within the framework of the thermionic theory to extract figures of merits such as the rectification ratio, the ideality factor, and the Schottky barrier height. The CNT/Si_3N_4/Si capacitor leads to the appearance of a kink in the reverse-bias *I–V* characteristics of the device, which is attributed to Fowler–Nordheim (FN) tunneling.[34] In such a way, when used as a photodetector, the device is endowed with extended functionalities compared to traditional photodiodes. The device shows a different photoresponse when light is focused on the CNT/Si_3N_4/Si region or around the Pt–Ti/Si_3N_4/Si MIS diode. Furthermore, the reverse bias can change the output photocurrent, suggesting that the device can be tailored to different applications, from voltage-tunable photodetection to Boolean logic. Finally, light generates a photocurrent at zero voltage and a photovoltage at zero current, making the device a self-powered photodetector.

2. Experimental Section

The CNT/Si_3N_4/Si capacitor was obtained by depositing a film of single-wall CNTs on a Si_3N_4/Si substrate, endowed with Pt–Ti/Si_3N_4/Si MIS structures, using a dry transfer process.[45] The substrate consists of an n-doped silicon wafer (300 µm thickness, 2300–3150 Ωcm resistivity) with the top surface covered by a 60 nm Si_3N_4 insulating layer. The back of the substrate is endowed with an ohmic Pt–Ti large area contact.

The top Pt–Ti pads (20 nm Ti/100 nm Pt) of the pre-existing MIS structure are used to contact the CNT film, which is patterned in a T-shape (see **Figure 1**). A 3D schematic view and a cross-section of the device are reported in Figure 1. The Pt–Ti/Si_3N_4/Si and CNT/Si_3N_4/Si heterostructures, after that the Si_3N_4 underneath the Pt–Ti pad had been broken by electrical stress, can be modeled as a MIS diode in parallel to a MIS capacitor, with a resistance in series (see Figure 1b). Indeed, the repeated electrical stress between the top Pt–Ti pad and the Si substrate makes the nitride barrier thinner, so that tunneling can occur, letting us model the Pt–Ti/Si_3N_4/Si structure as a stable MIS diode.[34,45–49]

Henceforth, we will refer to Pt–Ti/Si_3N_4/Si structure as the MIS diode and to CNT/Si_3N_4/Si structure as the MIS capacitor, while the parallel combination of the MIS diode and capacitor will be designated as the CNT–Si device.

The CNT film was obtained by filtering a liquid solution of CNTs through a filter membrane, in low vacuum. The liquid solution was made of CNT powder diluted to 80 µg mL^{-1} with distilled water and sodium dodecyl sulfate (SDS, 2% solution weight ratio), which surrounds the CNTs and prevents their aggregation and precipitation. The mixture was then tip-ultrasonicated for 1 h and left for about 10 h to let the bundled nanotubes precipitate, which is removed until getting a stable mixture without any kind of further CNT precipitation (it requires several months). Once we obtained a stable mixture, it was deposited on a filter membrane (Durapore PVDF, pore size 0.22 µm, diameter 47 mm) using vacuum filtration and rinsed with a solution of ethanol, methanol, and water (15%–15%–70%) to remove all the surfactant from the CNT film.

After the CNT filter was dried, we started the transfer process. The transfer is accomplished by placing a piece of CNT film over the substrate, wetting the membrane with water and ethanol, and then pressing it to improve the adhesion of the film to the substrate. After few minutes, the dried membrane was peeled off and the CNT film was left over the substrate.

The electrical measurements were realized in a Janis 500 high vacuum cryogenic probe station connected to a semiconductor parameter analyzer Keithley 4200-SCS. The photoresponse was investigated using a super continuous light source (1 mm^2 spot) with a wavelength in the 450–2400 nm range (SuperK compact by NKT photonics) as light source, which was focused either around the Pt–Ti pad or over the CNT film.

The morphology of the film was checked using a field-emission scanning electron microscope (Zeiss LEO 1530) using an acceleration voltage of 5 kV. **Figure 2**a shows the border of the CNT film above the silicon nitride surface (clearly visible on the bottom of the image). The film is homogeneous and does not present visible holes. Figure 2b shows the film at higher magnification, revealing that the nanotubes are randomly oriented and form a network that covers completely the substrate.

The film was analyzed with an X-ray photoelectron spectroscope (PHI 1257, using Al Kα radiation) to get information about its chemical composition and with micro-Raman (LABRAM, $\lambda = 633$ nm) to estimate the quality and the nature of the nanotubes. Figure 2c shows an XPS survey spectrum acquired on the film. The only observable signals came from the carbon, due to the nanotubes, and oxygen, that can be attributed to atmospheric contaminant above the film. Silicon signals are not observable, indicating once more the high level of coverage of the film. Figure 2d shows the Raman spectra acquired on the film. In the high-frequency region, we can

 © 2022 The Authors. Advanced Electronic Materials published by Wiley-VCH GmbH

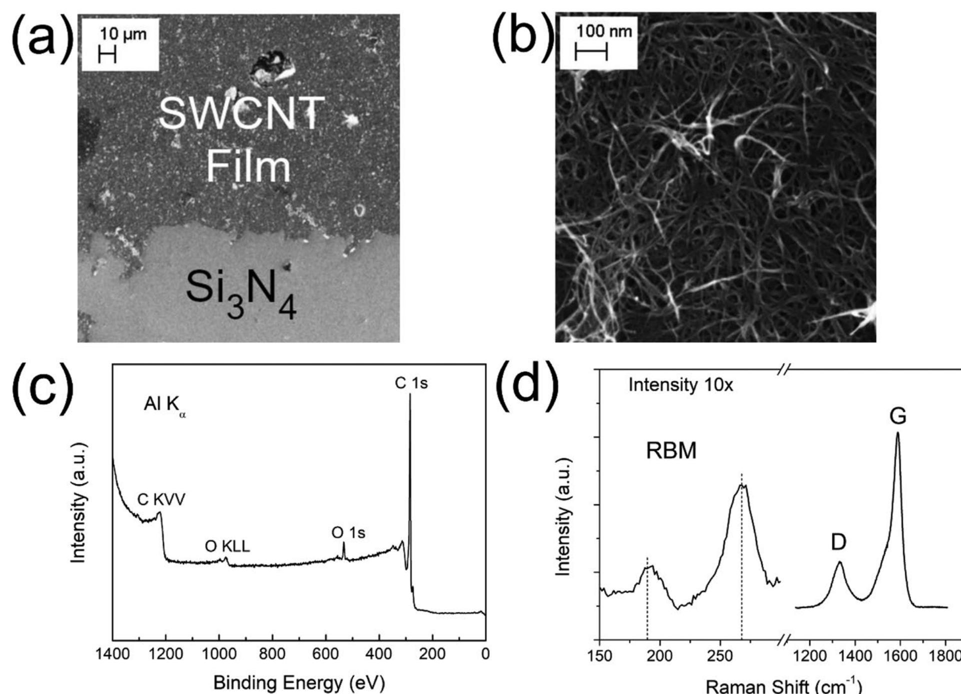

Figure 2. a) SEM image of the CNT film above the substrate at low magnification. b) Single-walled CNT film at high magnification. c) XPS survey spectrum and d) RAMAN spectrum of the CNT film.

observe the D and G bands typical of carbon materials, while in the low-frequency region are the radial breathing mode (RBM) of the single-walled CNT. The D band, that is due the presence of amorphous carbon and crystallographic defects, is less intense than the G band. This highlights the good quality of the nanotubes used for the film.

Using the frequency of the RBM we estimate the diameter of the nanotubes using the following relation:

$$d\,(\text{nm}) = \frac{234}{\omega\left(\text{cm}^{-1}\right) - 10} \tag{1}$$

The evaluated diameter allowed us to determine the chiral vector index and the type of the nanotubes (**Table 1**).

3. Results and Discussion

We measured the current–voltage characteristic of the single-walled CNT film using the two Pt–Ti pads over the Si_3N_4/Si connecting CNT film (Figure 1a) as the anode and the cathode, respectively. **Figure 3**a shows a linear behavior and a resistance of 177 kΩ suggesting the formation of good ohmic contacts between the pads and the CNT film.

Table 1. Frequency of the main RBM with the evaluated diameter, chiral vector index (*n*,*m*), and type of nanotubes.

ω [cm^{-1}]	*d* [nm]	(*n*,*m*)	Type
189.5	1.303	(14,4)	Semiconductor
267.7	0.908	(8,5)	Metallic

Conversely, Figure 3b shows the semilogarithmic plot of the *I*–*V* characteristic, measured between a top Pt–Ti pad and the back of the substrate, in dark at 300 K and atmospheric pressure. The *I*–*V* characteristic, which refers to the CNT–Si device consisting of the MIS diode and MIS capacitor in parallel, exhibits a rectifying behavior with a rectification ratio of about 10^3 at $V = \pm 4$ *V*. Such a curve was obtained after a series of electrical stresses that broke the Si_3N_4 underneath the Pt–Ti pad that was used to force the voltage.

To evaluate the MIS diode parameters, like the ideality factor and Schottky barrier height (SBH), we measured the output characteristics at different temperatures. To understand the role of the CNTs, we also studied a similar device (Ag–Si device), obtained by substituting the CNT layer with an Ag film. The corresponding *I*–*V* characteristics are displayed in **Figure 4**. The plots show that for both the CNT–Si and Ag–Si devices, comprising of the CNT or the Ag MIS capacitor in parallel to the MIS diode, there is a suppression of both the forward and reverse currents at low temperature, as predicted by the thermionic theory. However, the reverse current of the CNT–Si device shows a step up around $V = -7$ V at any temperature, that is not seen in the Ag–Si device.

A possible explanation is that the CNTs, due to their aspect ratio, can locally enhance the electric field and activate FN tunneling through the Si_3N_4 layer in the CNT-device capacitor.[48,50,51] The transition to the FN regime (corresponding to Zone II in Figure 4) occurs at any temperature when the reverse voltage is less than −7 V. Such a regime is not observed in the Ag–Si device because there is no field amplification and carriers might not be able to tunnel. The current saturation in the Zone II of Figure 4b is caused by the lump series resistance, due to substrate, contacts, and wires, which limits the current at higher bias.

 © 2022 The Authors. Advanced Electronic Materials published by Wiley-VCH GmbH

2199160x, 2023, 1, Downloaded from https://onlinelibrary.wiley.com/doi/10.1002/aelm.202200919 by CochraneItalia, Wiley Online Library on [28/02/2023]. See the Terms and Conditions (https://onlinelibrary.wiley.com/terms-and-conditions) on Wiley Online Library for rules of use; OA articles are governed by the applicable Creative Commons License

ADVANCED ELECTRONIC MATERIALS
www.advelectronicmat.de

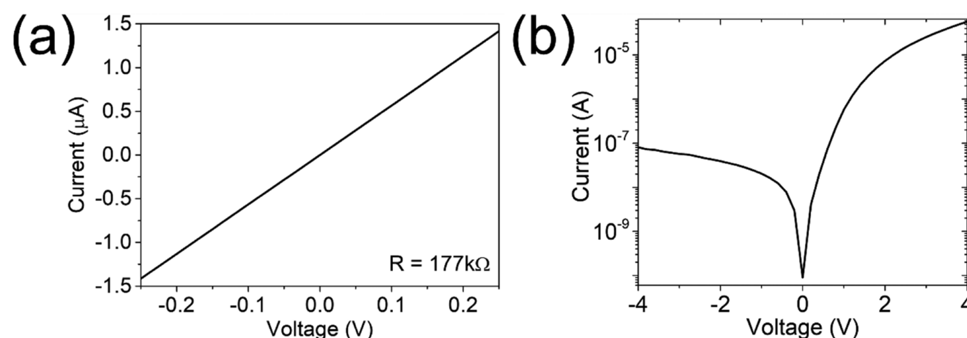

Figure 3. a) *I*–*V* characteristic of the CNT layer. b) Semilogarithmic plot of the *I*–*V* characteristic of the CNT–Si device.

Figure 5a shows the rectification (on/off) ratio at $V = \pm 4$ V for both devices as a function of the temperature. The decreasing trend with the rising temperature is due to the increased thermal generation that enhances the reverse current at higher temperatures. We note that the CNT–Si device shows an on/off ratio higher than the Ag–Si device, demonstrating that the use of a CNT film enhances the diode performance.

The *I*–*V* curves at different temperatures can be used to extract the SBH, ideality factor, and series resistance following Cheung's method.[52] We consider an ideal diode (MIS diode) with a resistance in series, as shown in Figure 1b. Then, the forward current can be expressed as

$$I = I_0 \exp\left(\frac{q(V - R_s I)}{nkT} - 1\right) \tag{2}$$

which, for $V - R_s I \gg nkT/q$, provides:

$$\frac{dV}{d(\ln I)} = R_s I + \frac{nkT}{q} \tag{3}$$

where R_s is the series resistance and n is the ideality factor. From the fit of Equation 3, we can evaluate R_s and n. With n known, we can estimate φ_B, that is the Schottky barrier height, form a linear fit of the $H(I)$–I plot, where the function $H(I)$ is defined as

$$H(I) = V - \frac{nkT}{q}\ln\left(\frac{I}{SA^*T^2}\right) = R_s I + \frac{n}{q}\varphi_B \tag{4}$$

Figure 5b–d shows the results obtained by applying Cheung's method. The temperature dependence of the ideality factor in Figure 5b shows a decreasing trend for increasing temperature. This feature indicates that deviations from the ideal thermionic behavior of the diode occur mainly at lower temperatures when thermionic emission is suppressed, and tunneling or diffusion might become comparatively relevant. Also, as expected, the ideality factor of both devices is almost the same. The forward current, indeed, is due, in both cases, to the MIS diode formed by the Pt–Ti/Si_3N_4/Si structure.

Figure 5c shows that the SBH, which is around 0.7 eV at room temperature, decreases with the decreasing temperature. We note that the obtained barrier is consistent with other works using similar devices.[53,54] The Schottky barrier height of the CNT–Si device is slightly lower than the Ag–Si device, but this can be attributed to the natural device-to-device fluctuations. Furthermore, the temperature behavior is a well-known effect when there is a spatial barrier inhomogeneity.[55–57] At low temperatures, the reduced thermal energy makes the carrier cross the barrier mainly in the positions where the SBH is lower, thus resulting in a reduced average SBH. Finally, Figure 5d shows the temperature behavior of the series resistance, which is almost constant over the explored temperature range. The lower series resistance of the CNT–Si device highlights another advantage of using the CNT film.

We tested the optical response of the CNT–Si device under illumination by a supercontinuum white source (8 mW cm^{-2} intensity) with the light spot focused over the MIS capacitor or over the MIS diode at room temperature. **Figure 6**a shows the resulting *I*–*V* characteristics in the dark and under the light. When the light is focused on the MIS diode, a high photocurrent due to photogeneration in the depletion region of the MIS diode appears already at low voltages (Zone I). At higher reverse voltages (Zone II), the photocurrent shows a further increase due

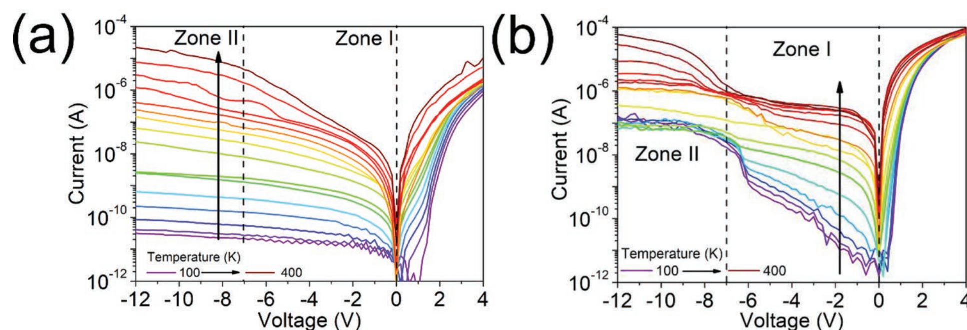

Figure 4. a,b) *I*–*V* characteristics at different temperatures for the Ag–Si device (a) and the CNT–Si device (b).

 © 2022 The Authors. Advanced Electronic Materials published by Wiley-VCH GmbH

2199160x, 2023, 1, Downloaded from https://onlinelibrary.wiley.com/doi/10.1002/aelm.202200919 by CochraneItalia, Wiley Online Library on [28/02/2023]. See the Terms and Conditions (https://onlinelibrary.wiley.com/terms-and-conditions) on Wiley Online Library for rules of use; OA articles are governed by the applicable Creative Commons License

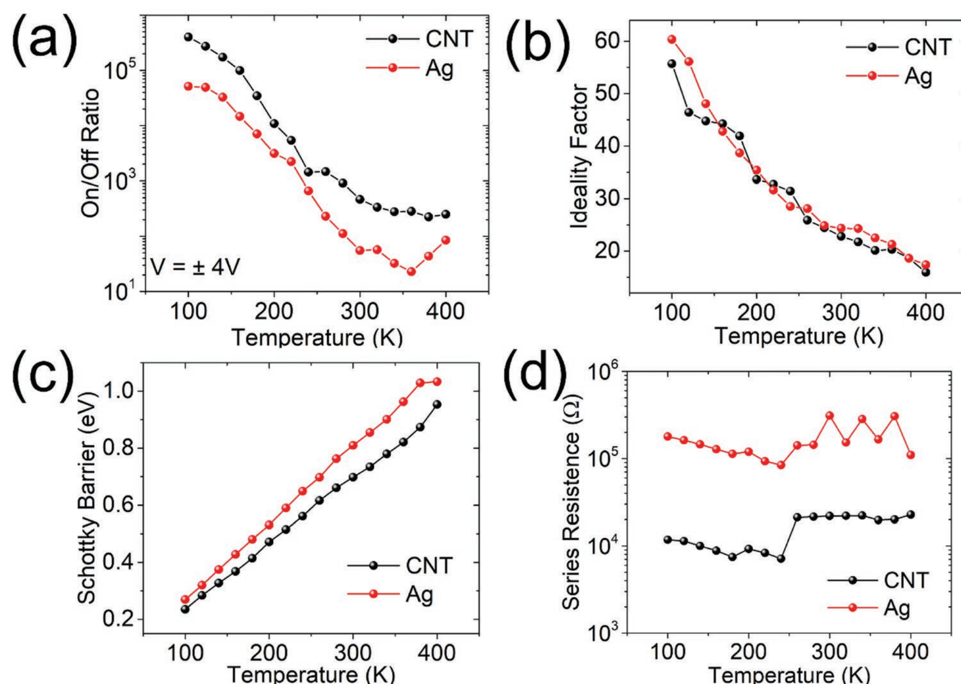

Figure 5. a) On/off ratio at V = ± 4V, b) ideality factor, c) Schottky barrier height, and d) series resistance, as a function of the temperature for the CNT–Si device (labeled as CNT, black) and the Ag–Si device (labeled as Ag, red).

to FN tunneling of charge photogenerated in the MIS capacitor region. Vice versa, when the light spot is on the MIS capacitor, the photocurrent mainly increases in Zone II, and is due to FN tunneling of the charge photogenerated in the area below the CNT capacitor. The total photocurrent is lower when the light spot is over the CNT MIS capacitor because of the thicker Si_3N_4 layer (the Si_3N_4 layer under the Pt–Ti pad is broken after the electrical stress).

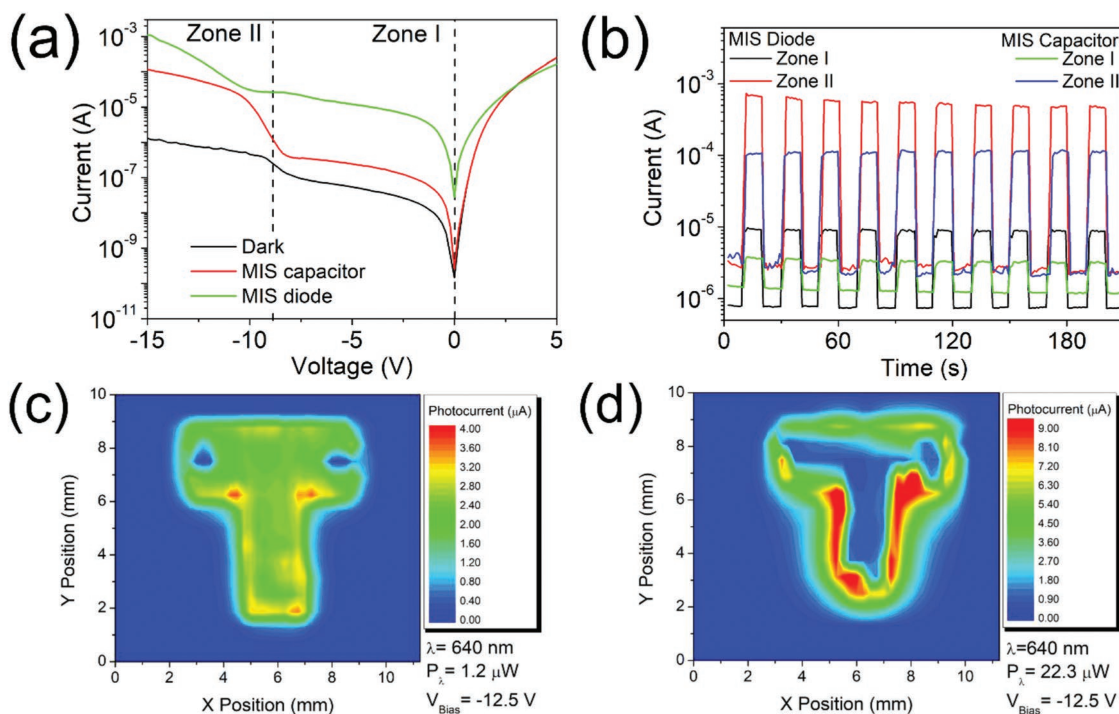

Figure 6. a) CNT–Si device *I–V* characteristics under illumination on the MIS diode (green curve) and the MIS capacitor (red curve). b) Extracted photocurrent at different biases and in different configurations. c) CNT-device and d) Ag-device photocurrent maps.

 © 2022 The Authors. Advanced Electronic Materials published by Wiley-VCH GmbH

2199160x, 2023, 1, Downloaded from https://onlinelibrary.wiley.com/doi/10.1002/aelm.202200919 by CochraneItalia, Wiley Online Library on [28/02/2023]. See the Terms and Conditions (https://onlinelibrary.wiley.com/terms-and-conditions) on Wiley Online Library for rules of use; OA articles are governed by the applicable Creative Commons License

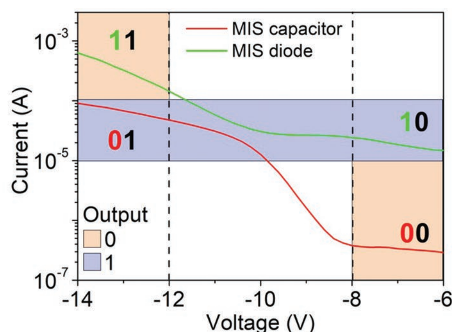

x (V_{bias})	y (Light on)	$x \oplus y$
-8V<V<-6V	MIS capacitor	0
-8V<V<-6V	MIS diode	1
-14V<V<-12V	MIS capacitor	1
-14V<V<-12V	MIS diode	0

Figure 7. CNT–Si device suitable for optoelectronic Boolean logic application, working as a XOR.

We point out that Zone I and II represent voltage ranges with two different output photocurrents. This behavior allows the photosensor to be operated in two different current regimes according to the requirement of the specific application.

Remarkably, Figure 6b, that shows the photocurrent at different negative biases, confirms that the photoresponse is faster than the limit of 500 ms set by our measurement setup, no matter if the light is focused around the Pt–Ti pad or the CNT film.

Figure 6c,d shows the photocurrent maps of the CNT–Si and the Ag–Si devices in Zone II (at $V = -12.5$ V) and fixed wavelength and incident power ($\lambda = 640$ nm; $P_\lambda = 1.2$ µW). The CNT film enhances the photoresponse of the device, extending the photosensitive area to the entire "*T*", while the Ag paste shuts out the light under the "*T*", thus resulting in suppressed photocurrent (even with increased light incident power, $P_\lambda = 22.3$ µW).

Furthermore, the photocurrent dependent on the voltage bias and the light spot position leads to a device for Boolean logic applications. Indeed, we can associate a binary variable (x) to the applied voltage V_{bias} (for instance, with value "0" for -8 V < V < -6 V and "1" for -14 V < V < -12 V), and a second variable (y) to the position of the incident light spot ("0" for the light spot over the MIS capacitor, "1" for the light spot over the MIS diode). **Figure 7** shows that the device can operate as an exclusive OR (XOR). Indeed, when the photocurrent is in the range 10^{-5} A < I < 10^{-4} A, the output is assumed to be "1", while elsewhere it is considered as a "0". We remark that the position of the light spot as a variable for a Boolean device is an original approach in our study.

We completed the optoelectronic characterization of the CNT–Si device, investigating the spectral response in the 500–1100 nm wavelength range by sampling the spectrum of the supercontinuum source in intervals of 50 nm with 20 nm bandwidth at room temperature. **Figure 8**a reports the responsivity of the device, defined as the ratio of photocurrent to the incident power, $R = \frac{I_{\text{light}} - I_{\text{dark}}}{P_\lambda}$, along with the external quantum

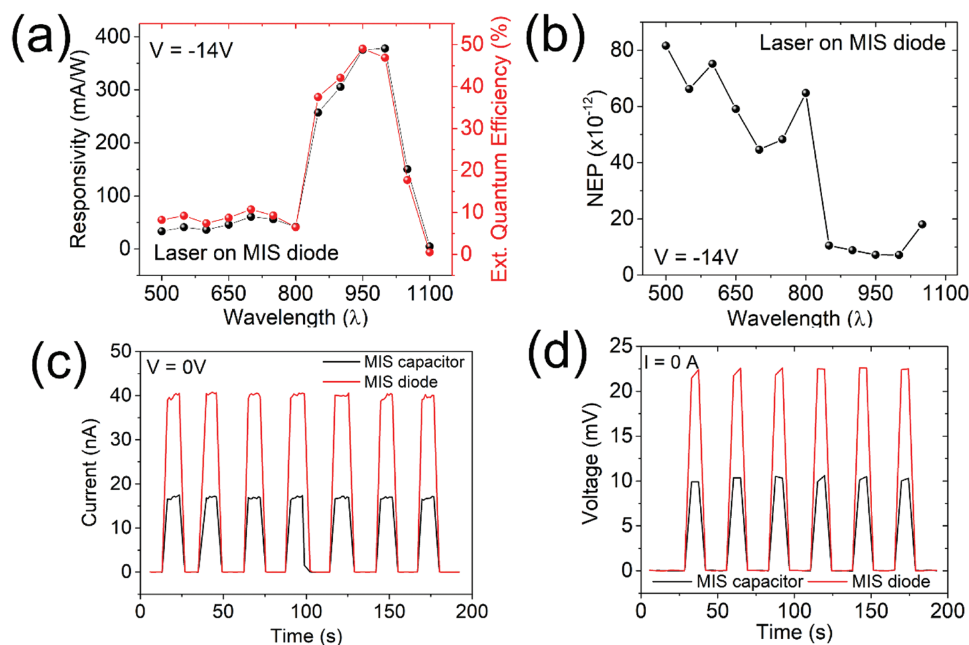

Figure 8. a) Responsivity and external quantum efficiency, b) noise equivalent power, c) photocurrent at 0 V, and d) photovoltage at 0 A of the CNT–Si device.

 © 2022 The Authors. Advanced Electronic Materials published by Wiley-VCH GmbH

2199160x, 2023, 1, Downloaded from https://onlinelibrary.wiley.com/doi/10.1002/aelm.202200919 by CochraneItalia, Wiley Online Library on [28/02/2023]. See the Terms and Conditions (https://onlinelibrary.wiley.com/terms-and-conditions) on Wiley Online Library for rules of use; OA articles are governed by the applicable Creative Commons License

efficiency, $\mathrm{EQE} = \frac{Rhc}{\lambda e}$ ($I_{\mathrm{light/dark}}$ is the current under illumination or in dark and P_λ is the incident optical power, λ is the wavelength, h is the Plank constant, c the speed of light and e the electron charge) at the applied voltage of $V = -14$ V (Zone II) and with light focused on the MIS diode. Figure 8a shows a peak in EQE around 50% for 800 nm < λ < 1100 nm suggesting that photoconversion occurs mainly in Si. The weaker photoresponse for λ < 800 nm can be attributed to the increased electron–hole recombination rate. High energy light is absorbed closer to the Si/Si_3N_4 interface where the high concentration of intragap states and the lower mobility favor the recombination of photogenerated electron–hole pairs. As an additional figure of merit, Figure 8b shows the noise equivalent power (NEP) that indicates the minimum detectable power. As expected, the higher quantum efficiency corresponds to the lower detection power. The obtained EQE is on the low side of the distribution of values typically reported in the literature.[58,59]

Setting the voltage to $V = 0$ V, we performed a series of measurements exposing the CNT–Si device to light, with the beam spot focused on the MIS diode. The device reacts to light with fast and repeatable photocurrent (Figure 8c). Furthermore, at zero current, we also observed a photovoltaic effect as reported in Figure 8d. Figure 8c,d shows that under illumination, the device generates both a current and a voltage, specifically 40 nA at 0 V and 20 mV at 0 A, when illuminated by white source at 8 mW cm^{-2} intensity, thus resulting in a photocurrent responsivity of 4.5 µA W^{-1} and a photovoltage responsivity (defined as $R = \frac{V_{\mathrm{light}} - V_{\mathrm{dark}}}{P_\lambda}$) of 2.5 V W^{-1}. Hence, the device can be operated in a self-powered mode.[60–62]

4. Conclusions

We fabricated a photodetector with a $CNT/Si_3N_4/Si$ MIS capacitor in parallel with a $Pt–Ti/Si_3N_4/Si$ MIS diode. The whole device shows rectifying *I–V* characteristics after electrical stress corresponding to the breakdown of the Si_3N_4 layer of the $Pt–Ti/Si_3N_4/Si$ MIS. The electric characterization shows an increasing current with the raising temperature, consistently with the thermionic emission theory. The temperature behavior highlights a decreasing rectification ratio and ideality factor, and an increasing Schottky barrier. The CNT film increases the performance of the MIS diode and enhances the photosensitive area of the photodetector. More importantly, it enables two different current regimes in reverse bias. The bias-dependent output photocurrent makes the photodetector suitable to different applications, such as voltage bias tunable photodetector or optoelectronic Boolean logic circuits. Finally, under illumination the device generates both a current and a voltage, therefore it can be operated in self-powered mode.

Acknowledgements

A.D.B. thanks the University of Salerno, Salerno, Italy, for the grants ORSA223384 and ORSA218189.

Note: Marking to indicate Antonio Di Bartolomeo as a second corresponding author was added on January 10, 2023, after initial publication online.

Conflict of Interest

The authors declare no conflict of interest.

Data Availability Statement

The data that support the findings of this study are available from the corresponding author upon reasonable request.

Keywords

capacitors, carbon nanotubes, diodes, heterojunctions, MIS structures, photodetectors, self-powered devices

Received: August 12, 2022
Revised: September 29, 2022
Published online: November 9, 2022

[1] G. Lamura, A. Andreone, Y. Yang, P. Barbara, B. Vigolo, C. Hérold, J.-F. Marêché, P. Lagrange, M. Cazayous, A. Sacuto, M. Passacantando, F. Bussolotti, M. Nardone, *J. Phys. Chem. C* **2007**, *111*, 15154.
[2] Y. R. Poudel, W. Li, *Mater. Today Phys.* **2018**, *7*, 7.
[3] T. Belin, F. Epron, *Mater. Sci. Eng., B* **2005**, *119*, 105.
[4] G. Gorrasi, V. Bugatti, C. Milone, E. Mastronardo, E. Piperopoulos, L. Iemmo, A. Di Bartolomeo, *Composites, Part B* **2018**, *135*, 149.
[5] L. Guadagno, M. Raimondo, C. Naddeo, A. Di Bartolomeo, K. Lafdi, *J. Polym. Sci. B: Polym. Phys.* **2012**, *50*, 963.
[6] V. Bugatti, G. Viscusi, A. Di Bartolomeo, L. Iemmo, D. C. Zampino, V. Vittoria, G. Gorrasi, *Polymers* **2020**, *12*, 495.
[7] S. Kruss, A. J. Hilmer, J. Zhang, N. F. Reuel, B. Mu, M. S. Strano, *Adv. Drug Delivery Rev.* **2013**, *65*, 1933.
[8] C. Giordano, G. Filatrella, M. Sarno, A. Di Bartolomeo, *Micro & Nano Lett.* **2019**, *14*, 304.
[9] I. V. Zaporotskova, N. P. Boroznina, Y. N. Parkhomenko, L. V. Kozhitov, *Modern Electron. Mater.* **2016**, *2*, 95.
[10] A. D. Bartolomeo, M. Rinzan, A. K. Boyd, Y. Yang, L. Guadagno, F. Giubileo, P. Barbara, *Nanotechnology* **2010**, *21*, 115204.
[11] C. Dekker, *Nat. Electron.* **2018**, *1*, 518.
[12] U. Coscia, G. Ambrosone, A. Ambrosio, M. Ambrosio, F. Bussolotti, V. Carillo, V. Grossi, P. Maddalena, M. Passacantando, E. Perillo, A. Raulo, S. Santucci, *Solid State Sci.* **2009**, *11*, 1806.
[13] A. Di Bartolomeo, Y. Yang, M. B. M. Rinzan, A. K. Boyd, P. Barbara, *Nanoscale Res. Lett.* **2010**, *5*, 1852.
[14] M. Passacantando, F. Bussolotti, S. Santucci, A. Di Bartolomeo, F. Giubileo, L. Iemmo, A. M. Cucolo, *Nanotechnology* **2008**, *19*, 395701.
[15] F. Giubileo, L. Iemmo, G. Luongo, N. Martucciello, M. Raimondo, L. Guadagno, M. Passacantando, K. Lafdi, A. Di Bartolomeo, *J. Mater. Sci.* **2017**, *52*, 6459.
[16] P. Li, Y. Wang, M. Zhang, L. Wu, X.-X. Yu, *Carbon* **2020**, *159*, 1.
[17] Y. Zhang, Y. Wang, *RSC Adv.* **2017**, *7*, 45129.
[18] F. Urban, F. Gity, P. K. Hurley, N. McEvoy, A. Di Bartolomeo, *Appl. Phys. Lett.* **2020**, *117*, 193102.
[19] A. Grillo, E. Faella, A. Pelella, F. Giubileo, L. Ansari, F. Gity, P. K. Hurley, N. McEvoy, A. Di Bartolomeo, *Adv. Funct. Mater.* **2021**, *31*, 2105722.

 © 2022 The Authors. Advanced Electronic Materials published by Wiley-VCH GmbH

2199160x, 2023, 1, Downloaded from https://onlinelibrary.wiley.com/doi/10.1002/aelm.202200919 by CochraneItalia, Wiley Online Library on [28/02/2023]. See the Terms and Conditions (https://onlinelibrary.wiley.com/terms-and-conditions) on Wiley Online Library for rules of use; OA articles are governed by the applicable Creative Commons License

[20] L. Prechtel, L. Song, S. Manus, D. Schuh, W. Wegscheider, A. W. Holleitner, *Nano Lett.* **2011**, *11*, 269.
[21] D. Melisi, M. A. Nitti, M. Valentini, A. Valentini, T. Ligonzo, G. D. Pascali, M. Ambrico, *Beilstein J. Nanotechnol.* **2014**, *5*, 1999.
[22] A. Tinti, F. Righetti, T. Ligonzo, A. Valentini, E. Nappi, A. Ambrosio, M. Ambrosio, C. Aramo, P. Maddalena, P. Castrucci, M. Scarselli, M. De Crescenzi, E. Fiandrini, V. Grossi, S. Santucci, M. Passacantando, *Nucl. Instrum. Methods Phys. Res., Sect. A* **2011**, *629*, 377.
[23] M. Passacantando, F. Bussolotti, V. Grossi, S. Santucci, A. Ambrosio, M. Ambrosio, G. Ambrosone, V. Carillo, U. Coscia, P. Maddalena, E. Perillo, A. Raulo, *Appl. Phys. Lett.* **2008**, *93*, 051911.
[24] M. Passacantando, V. Grossi, S. Santucci, *Appl. Phys. Lett.* **2012**, *100*, 163119.
[25] A. Di Bartolomeo, *Phys. Rep.* **2016**, *606*, 1.
[26] M. Scagliotti, M. Salvato, F. Frezza, D. Catone, L. Di Mario, M. Boscardin, M. De Crescenzi, P. Castrucci, *Appl. Sci.* **2021**, *11*, 606.
[27] Y. Jia, A. Cao, X. Bai, Z. Li, L. Zhang, N. Guo, J. Wei, K. Wang, H. Zhu, D. Wu, P. M. Ajayan, *Nano Lett.* **2011**, *11*, 1901.
[28] X. Li, Z. Lv, H. Zhu, *Adv. Mater.* **2015**, *27*, 6549.
[29] C. Aramo, A. Ambrosio, M. Ambrosio, M. Cilmo, F. Guarino, P. Maddalena, V. Grossi, M. Passacantando, S. Santucci, E. Nappi, A. Tinti, A. Valentini, E. Fiandrini, G. Pignatel, P. Castrucci, M. De Crescenzi, M. Scarselli, in *Astroparticle, Particle, Space Physics and Detectors for Physics Applications*, World Scientific, Singapore **2012**, p. 822.
[30] J. Diao, D. Srivastava, M. Menon, *J. Chem. Phys.* **2008**, *128*, 164708.
[31] X. Li, M. Mariano, L. McMillon-Brown, J.-S. Huang, M. Y. Sfeir, M. A. Reed, Y. Jung, A. D. Taylor, *Small* **2017**, *13*, 1702387.
[32] A. Pelella, A. Grillo, E. Faella, G. Luongo, M. B. Askari, A. Di Bartolomeo, *ACS Appl. Mater. Interfaces* **2021**, *13*, 47895.
[33] X. Hu, P. Hou, C. Liu, H. Cheng, *Nano Mater. Sci.* **2019**, *1*, 156.
[34] A. Di Bartolomeo, F. Giubileo, A. Grillo, G. Luongo, L. Iemmo, F. Urban, L. Lozzi, D. Capista, M. Nardone, M. Passacantando, *Nanomaterials* **2019**, *9*, 1598.
[35] A. D. Bartolomeo, G. Luongo, F. Giubileo, N. Funicello, G. Niu, T. Schroeder, M. Lisker, G. Lupina, *2D Mater.* **2017**, *4*, 025075.
[36] S. Riazimehr, S. Kataria, R. Bornemann, P. Haring Bolívar, F. J. G. Ruiz, O. Engström, A. Godoy, M. C. Lemme, *ACS Photonics* **2017**, *4*, 1506.
[37] S. Riazimehr, M. Belete, S. Kataria, O. Engström, M. C. Lemme, *Adv. Opt. Mater.* **2020**, *8*, 2000169.
[38] S. Riazimehr, S. Kataria, J. M. Gonzalez-Medina, S. Wagner, M. Shaygan, S. Suckow, F. G. Ruiz, O. Engström, A. Godoy, M. C. Lemme, *ACS Photonics* **2019**, *6*, 107.
[39] G. Luongo, A. D. Bartolomeo, F. Giubileo, C. A. Chavarin, C. Wenger, *J. Phys. D: Appl. Phys.* **2018**, *51*, 255305.
[40] W. Ouyang, F. Teng, J.-H. He, X. Fang, *Adv. Funct. Mater.* **2019**, *29*, 1807672.
[41] Y. Jia, A. Cao, F. Kang, P. Li, X. Gui, L. Zhang, E. Shi, J. Wei, K. Wang, H. Zhu, D. Wu, *Phys. Chem. Chem. Phys.* **2012**, *14*, 8391.
[42] A. Filatzikioti, N. Glezos, V. Kantarelou, A. Kyriakis, G. Pilatos, G. Romanos, T. Speliotis, D. J. Stathopoulou, *Solid-State Electron.* **2019**, *151*, 27.
[43] K. A. Shah, M. S. Parvaiz, G. N. Dar, P. Misra, *J. Appl. Phys.* **2022**, *131*, 204301.
[44] Y. L. Kim, H. Y. Jung, S. Park, B. Li, F. Liu, J. Hao, Y.-K. Kwon, Y. J. Jung, S. Kar, *Nat. Photonics* **2014**, *8*, 239.
[45] D. Capista, M. Passacantando, L. Lozzi, E. Faella, F. Giubileo, A. Di Bartolomeo, *Electronics* **2022**, *11*, 271.
[46] A. Buyukbas-Ulusan, A. Tataroglu, *J. Mater. Sci.: Mater. Electron.* **2020**, *31*, 9888.
[47] F. Z. Pür, A. Tataroğlu, *Phys. Scr.* **2012**, *86*, 035802.
[48] A. Di Bartolomeo, H. Rücker, P. Schley, A. Fox, S. Lischke, K.-Y. Na, *Solid-State Electron.* **2009**, *53*, 644.
[49] F. Yigiterol, H. H. Güllü, Ö. Bayraklı, D. E. Yıldız, *J. Electron. Mater.* **2018**, *47*, 2979.
[50] A. Di Bartolomeo, A. Scarfato, F. Giubileo, F. Bobba, M. Biasiucci, A. M. Cucolo, S. Santucci, M. Passacantando, *Carbon* **2007**, *45*, 2957.
[51] A. Grillo, M. Passacantando, A. Zak, A. Pelella, A. Di Bartolomeo, *Small* **2020**, *16*, 2002880.
[52] S. K. Cheung, N. W. Cheung, *Appl. Phys. Lett.* **1986**, *49*, 85.
[53] K. Ertürk, Y. Bektöre, M. C. Haciismailoglu, *Phys. Status Solidi C* **2005**, *2*, 1428.
[54] A. Tataroğlu, F. Z. Pür, *Phys. Scr.* **2013**, *88*, 015801.
[55] A. D. Bartolomeo, F. Giubileo, G. Luongo, L. Iemmo, N. Martucciello, G. Niu, M. Fraschke, O. Skibitzki, T. Schroeder, G. Lupina, *2D Mater.* **2016**, *4*, 015024.
[56] D. Tomer, S. Rajput, L. J. Hudy, C. H. Li, L. Li, *Nanotechnology* **2015**, *26*, 215702.
[57] J. H. Werner, H. H. Güttler, *J. Appl. Phys.* **1991**, *69*, 1522.
[58] M. Salvato, M. Scagliotti, M. D. Crescenzi, M. Crivellari, P. Prosposito, I. Cacciotti, P. Castrucci, *Nanotechnology* **2017**, *28*, 435201.
[59] D. H. Shin, S.-H. Choi, *Micromachines* **2018**, *9*, 350.
[60] P. Lv, X. Zhang, X. Zhang, W. Deng, J. Jie, *IEEE Electron Device Lett.* **2013**, *34*, 1337.
[61] D. Periyanagounder, P. Gnanasekar, P. Varadhan, J.-H. He, J. Kulandaivel, *J. Mater. Chem. C* **2018**, *6*, 9545.
[62] M. Fidan, Ö. Ünverdi, C. Çelebi, *Sens. Actuators, A* **2021**, *331*, 112829.

 © 2022 The Authors. Advanced Electronic Materials published by Wiley-VCH GmbH

2199160x, 2023, 1, Downloaded from https://onlinelibrary.wiley.com/doi/10.1002/aelm.202200919 by CochraneItalia, Wiley Online Library on [28/02/2023]. See the Terms and Conditions (https://onlinelibrary.wiley.com/terms-and-conditions) on Wiley Online Library for rules of use; OA articles are governed by the applicable Creative Commons License